Journal of Energy Storage 77 (2024) 109926

Contents lists available at ScienceDirect

Journal of Energy Storage

journal homepage: www.elsevier.com/locate/est

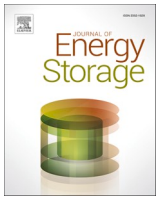

Research papers

Electrochemical performances and Li^+-storage mechanism of highly proportional 1T-MoS_2/hierarchical porous activated carbon nanocomposites

Mohamed M. Abdelaal [a,b], Chun-Chen Yang [a,c,d], Tai-Feng Hung [a,*]

[a] Battery Research Center of Green Energy, Ming Chi University of Technology, New Taipei City 24301, Taiwan
[b] Tabbin Institute for Metallurgical Studies (TIMS), Cairo 11421, Egypt
[c] Department of Chemical Engineering, Ming Chi University of Technology, New Taipei City 24301, Taiwan
[d] Department of Chemical and Materials Engineering, Chang Gung University, Taoyuan 33302, Taiwan

ARTICLE INFO

Keywords:
1T-MoS_2
Hierarchical porous activated carbon
Lithium-ion storage
Pseudocapacitive contribution
Clean energy technology

ABSTRACT

The metallic phase of molybdenum disulfide (1T-MoS_2) shows distinct advantages for lithium storage owing to its superior electronic conductivity, abundance of electroactive sites, and wider interplanar spacing compared to the semiconducting phase (2H-MoS_2). However, investigating lithium storage in 1T-MoS_2 encounters significant challenges attributed to its thermodynamic instability during synthesis and its transformation to an amorphous structure following the irreversible conversion reaction. This study addresses these challenges by utilizing hierarchical porous activated carbon (HPAC) to achieve the highest reported proportion (85 %) of 1T-MoS_2 and by restricting the potential window to induce selective intercalation reaction. Impressively, 1T-MoS_2/HPAC anodes exhibit a reversible capacity that surpasses the theoretical capacity (167 mAh/g) at various current densities from 0.1 to 2.0 A/g. This superior performance extends even after 100 cycles, retaining a capacity of 276 mAh/g at 0.1 A/g. The kinetic analysis indicates that the additional capacity originated from non-Faradic lithium storage, reaching 96 % at 5.0 mV/s. Further studies employing *ex-situ* XRD and *in-situ* EIS at various lithiation depths unveil the formation of a novel permanent phase after lithiation, characterized by expanded interlayer spacing and improved conductivity compared to the un-lithiated material. These findings open promising avenues for developing anode materials for lithium-ion batteries/capacitors applications.

1. Introduction

Molybdenum disulfide (MoS_2) has garnered significant attention as a promising anode material for lithium storage due to its high theoretical capacity and the layered structure featuring a wide interplanar spacing (approximately 0.62 nm) [1,2]. The notable combination of high ionic diffusion and significant pseudocapacitive contribution endows MoS_2-based anodes to exhibit rapid kinetic even at high charge/discharge rates [3,4]. In particular, the metallic phase of MoS_2, referred to as 1T-MoS_2, has demonstrated remarkable electrochemical performance in lithium-ion storage compared to its semiconductor counterpart, the 2H-MoS_2 phase [5,6]. This superiority can be attributed to the exceptional electronic conductivity exhibited by 1T-MoS_2, boosting a conductivity approximately 10^7 times greater than 2H-MoS_2 [7,8]. Furthermore, 1T-MoS_2 possesses significantly wider interlayer spacing (reaching 0.99 nm in some reports), facilitating ion diffusion during cycling [5,8,9].

Moreover, the 1T-MoS_2 shows a high tendency towards lithium-ion, as calculated by density functional theory (DFT) [10–12]. The 1T-phase displays a higher binding energy for lithium adsorption than the 2H-phase (−3.02 eV *vs.* −1.97 eV, respectively) since the greater negative adsorption energy reflects a more stable binding property [10–12]. Moreover, nitrogen-doped and sulfur vacancy in MoS_2 lattice provide extra electrochemical active sites for lithium storage with the binding energy of −2.25 eV *vs.* −2.95 eV, respectively [1]. Additionally, the binding energy of lithium on the edges is greater than that on the basal plane [10]. This suggests that a greater quantity of edge sites in nitrogen-doped 1T-MoS_2 with sulfur vacancies enhances the strength of the binding interaction with lithium ions, providing significant pseudocapacitive behavior [1,10].

Similar to other MoS_2, the 1T-MoS_2 stores lithium through

* Corresponding author.
E-mail address: taifeng@mail.mcut.edu.tw (T.-F. Hung).

https://doi.org/10.1016/j.est.2023.109926
Received 7 September 2023; Received in revised form 1 November 2023; Accepted 30 November 2023
Available online 5 December 2023
2352-152X/© 2023 Elsevier Ltd. All rights reserved.

intercalation (Eq. (1)) and conversion reactions (Eq. (2)), offering a high theoretical capacity of 669 mAh/g as follows [2,10]:

$$MoS_2 + xLi^+ + xe^- \rightarrow Li_xMoS_2 \text{ (Intercalation reaction)} \quad (1)$$

$$Li_xMoS_2 + (4-x)Li^+ + (4-x)e^- \rightarrow Mo + 2Li_2S \text{ (Conversion reaction)} \quad (2)$$

Nevertheless, the practical implementation of MoS_2 and other metal sulfide-based anode materials encounter obstacles due to the irreversible nature of the conversion reaction, resulting in rapid capacity fading [10,13]. Additionally, the conversion reaction results in diminished X-ray diffraction (XRD) peaks of 1T-MoS_2, complicating the investigation of phase changes during cycling. Previous research has attempted to avoid the conversion reaction by restricting the potential window to the intercalation reaction to improve cyclability [1,10,13]. However, the theoretical capacity of MoS_2 through one electron transfer during the intercalation reaction is only 167 mAh/g, which does not meet the capacity requirement of anode for lithium storage [10,13]. Practical capacity values reported in the literature range from 153 mAh/g to 191 mAh/g at 0.1 A/g through the intercalation reaction [2,14–16].

Investigation of lithium storage in 1T-MoS_2 has also been constrained by the limited proportion of 1T-phase, which tends to convert to the thermodynamically stable 2H-phase [6,17]. Previous studies have attempted to stabilize 1T-MoS_2 by electron donator to 4*d* orbital and by preventing the sliding of layered structure to 2H-phase [6,18]. For example, inserting alkali metals or protonated NH_4^+ has been shown to prevent the restacking of MoS_2 layers and maintain the octahedral structure of 1T-MoS_2 [6,18]. Wu et al. achieved uniform growth of 1T-MoS_2 on activated carbon fiber cloth, introducing DMF oxidized products between MoS_2 layers to stabilize the 1T phase, although subsequent calcination at 700 °C converted it to 2H-MoS_2 [19]. However, the calcination process is essential to improve the crystallinity of MoS_2, consequently increasing the intercalated lithium [3,4].

Herein, MoS_2 was successfully synthesized on a hierarchical porous activated carbon (HPAC) by microwave-assisted reaction and then calcined in nitrogen atmosphere. X-ray photoelectron spectroscopy (XPS) confirmed that the crystalline MoS_2/HPAC nanocomposites contained 85 % of 1T-phase, so-called 1T-MoS_2/HPAC. To the best of our knowledge, it is the highest percentage of 1T-phase MoS_2 reported in the literature. More interestingly, within the restricted potential window of 0.8 V ~ 3.0 V (*vs.* Li/Li^+), our 1T-MoS_2/HPAC delivered a reversible capacity of 338 mAh/g at 0.1 A/g, revealing the highest reported capacity within this potential window of the intercalation reaction. Such outstanding electrochemical performance raises the possibility of 1T-MoS_2/HPAC as a promising anode candidate for lithium storage, featuring remarkable reversible capacity.

2. Experimental section

2.1. Chemicals

The chemicals employed in this study were utilized as received without further purification. The hierarchical porous activated carbon (HPAC) was previously synthesized by our group through pyrolysis of the polyvinylpyrrolidone (PVP, average MW: 1,300,000, Sigma-Aldrich) hydrogel at 900 °C under an argon atmosphere flow for 2 h. As a result, HPAC exhibited a specific surface area of 2,012 m^2/g with predominant micropores. In addition, the volume of ultramicropores, micropores, and mesopores were determined to be 0.11, 0.69, and 0.47 cm^3/g, respectively, featuring with a hierarchical structure [20]. Ammonium molybdate tetrahydrate ($(NH_4)_6Mo_7O_{24}.4H_2O$, 81–83 % as MoO_4^-, Alfa Aesar), thioacetamide (CH_3CSNH_2, 98 %, Alfa Aesar), ethylene glycol ($C_2H_4(OH)_2$, Baker Analyzed™ reagent, J.T. Baker) were used in the synthesis of 1T-MoS_2/HPAC. Carbon black (Super P®, Timcal Ltd.), poly (vinylidene fluoride) (PVDF, Kynar® HSV 1800, Arkema Inc.), and *N*-methylpyrolidinone (NMP, ChromAR®, Macron Fine Chemicals™) were utilized in the electrode preparation.

2.2. Synthesis of 1T-MoS_2/HPAC nanocomposites

The synthesis process of the 1T-MoS_2/HPAC nanocomposites was described as follows. Initially, 0.05 g of HPAC was dispersed uniformly in a mixture of 20 mL of $C_2H_4(OH)_2$ and 20 mL of DI water using ultrasonication for 1 h. Then, 1 mmol of $(NH_4)_6Mo_7O_{24}.4H_2O$ were dissolved in the mixture with 35 mmol of CH_3CSNH_2 under continuous stirring for 1 h. The suspension was then heated in a microwave reactor under constant stirring (Discover® System, CEM Corporation, 2455 MHz). The microwave setting during the experiment was: an output power of 100 W, a reaction temperature of 150 °C, and a duration of 1 h. The product was filtered and rinsed repeatedly with DI water and ethanol. Subsequently, it was dried at 60 °C for 24 h. Finally, the crystallinity of 1T-MoS_2/HPAC was improved by calcination the dried product at 550 °C for 2 h under a nitrogen atmosphere with a flow rate of 200 mL/min. The same procedure was used to synthesize MoS_2 in the absence of HPAC for the purpose of comparing characterizations, so-called MoS_2.

2.3. Characterizations

The crystalline structures of the as-prepared powders and electrode were analyzed using an X-ray diffractometer (XRD, D2 PHASER, Bruker AXS Inc.) with a Cu target ($\lambda = 1.541$ Å) operating at 30 kV and 10 mA, with a scanning rate of 2.5 s/step. The XRD patterns were collected over a 2θ range of 10° to 80° for the powder samples and 5° to 20° for the electrode samples. Raman spectra were acquired using a Raman microscope (inVia, Renishaw, UK) equipped with a 633 nm laser source. Micrographs of the 1T-MoS_2/HPAC powder was obtained through scanning electron microscope (SEM, JSM-IT200, JEOL Ltd., Tokyo, Japan) and transmission electron microscopy (TEM, JEM-2100, JEOL Ltd., Japan). The chemical environment of the 1T-MoS_2/HPAC was investigated using X-ray photoelectron spectroscopy (XPS, PHI 5000 VersaProbe III, ULVAC-PHI, Inc., Japan) with a beam size of 100 μm under Al Kα radiation ($\lambda = 8.3406$ Å). An elemental analyzer (FLASH 2000, Thermo Fisher Scientific Inc., USA) was employed to determine the proportions of carbon, nitrogen, and sulfur within the 1T-MoS_2/HPAC.

2.4. Electrochemical measurements

For the preparation of the 1T-MoS_2/HPAC electrode, a slurry containing 70 wt% 1T-MoS_2/HPAC, 20 wt% Super P, and 10 wt% PVDF was applied onto a copper foil, while NMP was used to adjust the viscosity. Following drying at 60 °C for 24 h, the electrode film was calendared multiple times under ambient conditions. The mass loading and thickness of 1T-MoS_2/HPAC electrodes were 2.5 ± 0.2 mg/cm^2 and 25 ± 3 μm, respectively. For comparison, the HPAC electrodes (2.3 ± 0.1 mg/cm^2 in mass and 34 ± 2 μm in thickness) were also prepared using the same receipt and procedures.

The half cells were assembled using the 1T-MoS_2/HPAC electrode, lithium foil as a reference/counter electrode, 1.0 mol/L $LiPF_6$ in ethylene carbonate (EC)/diethyl carbonate (DEC) (1:1, v/v) as an electrolyte, and polyethylene as a separator. The coin cells were assembled in an argon-filled glovebox with oxygen and moisture levels maintained at <0.5 and 0.1 ppm, respectively. Electrochemical tests were conducted under ambient conditions within the potential range of 0.8 V ~ 3.0 V (*vs.* Li/Li^+). Cyclic voltammetry (CV) and electrochemical impedance spectroscopy (EIS) experiments were carried out using a multichannel electrochemical workstation (VSP-3e, Bio-Logic, France). EIS tests utilized an AC potential amplitude of 5 mV, with a frequency range from 100 kHz to 1.00 Hz. A computer-controlled charger (CT-4008T-5V50 mA, Neware Technology Limited) was used to measure the rate capabilities and cycling stability. The capacity values reported throughout this study were calculated based on the mass of 1T-MoS_2/HPAC. The kinetic analysis of the CV curves was performed using Eq. (3) [16]:

$$i(v) = k_1 v + k_2 v^{1/2} \quad (3)$$

where i(v) represents the total stored charge, and k_1v and k_2v symbolize the surface-controlled and diffusion-controlled processes as a function of a scanning rate (v), respectively. The differential capacity (dQ/dV) test was carried out at 0.1 A/g for the first couple of cycles, where dQ represents a slight change in charges, while dV represents a minor change in voltage [11].

3. Results and discussion

3.1. Characterizations of 1T-MoS_2/HPAC

The XRD pattern of the 1T-MoS_2/HPAC was compared to that of MoS_2, as shown in Fig. 1a. Both materials exhibited characteristic crystalline peaks of molybdenum disulfide (JCPDS card no. 37-1492) [21,22]. The distinct peak observed at a 2θ angle of 14.3° for MoS_2 corresponds to the (002) plane in the 2H-phase of molybdenum disulfide. In contrast, a significant difference was evident in the case of 1T-MoS_2/HPAC, where a broadened peak ranging from 2θ of 13° to 15° was observed. This indicates a change in the growth orientation of the MoS_2 crystalline planes within the hierarchical structure of HPAC. This broadening phenomenon has previously been reported in similar studies and suggests the formation of a few-layered structure [2,21]. The presence of these layered structures is advantageous for reducing the path length for lithium-ion movement during the lithiation and delithiation processes [2,23].

Similarly, micro-Raman spectroscopy was utilized to investigate the mixed (1T/2H) phases of MoS_2 in 1T-MoS_2/HPAC and the influence of HPAC on MoS_2 growth. Fig. 1b illustrates the Raman spectra obtained for 1T-MoS_2/HPAC, where the lower Raman shift reveals three distinct peaks located at 186.4, 223.8, and 348.9 cm^{-1}, corresponding to J_1, J_2, and J_3 vibrational modes, respectively. These peaks indicate the characteristic vibration modes of the 1T-phase MoS_2 [24,25]. Additionally, three peaks observed at 375.8, 401.5, and 450.4 cm^{-1} correspond to the phonon mode (E^1_{2g}), out-of-plane Mo—S mode (A_{1g}), and second-order Raman scattering 2LA(M), respectively, characterizing the 2H-phase MoS_2 [24,25]. Besides, two distinctive peaks at 1323.2 and 1578.6 cm^{-1} were observed, assigned to the disordered carbon (D-band) and graphitic layer (G-band) of the carbon [26–28]. In contrast, the MoS_2 exhibited obvious peaks of 2H-phase and unnoticeable peaks of 1T-phase MoS_2 with an absence of D- and G-bands, as illustrated in Fig. S1. This observation strongly suggests that HPAC played a substantial role in enriching 1T-phase MoS_2 during synthesis.

The SEM micrograph of 1T-MoS_2/HPAC accompanied by EDX mapping is shown in Fig. S2. It is clearly seen that the MoS_2 particles were fully covered over the HPAC (Fig. S2a), implying that the precursors of Mo and S were well-interacted with the HPAC. Accordingly, the intense signals of Mo and S were also revealed in Fig. S2b and S2c, respectively. However, fewer carbon (Fig. S2d) and nitrogen (Fig. S2e) signals were still detected, which were attributed to the presence of HAPC and nitrogen doping, respectively. TEM was used to investigate the crystal structures and orientations of MoS_2 in the as-synthesized 1T-MoS_2/HPAC, as depicted in Fig. 2. In particular, two distinct planes with different d-spacing were observed, measuring 0.81 nm and 0.63 nm, which can be attributed to the (001) plane of the 1T-phase and the (002) plane of the 2H-phase in MoS_2, respectively [18,25]. These values exceed those from the standard diffraction peaks, indicating an expanded interlayer spacing that enhances the insertion and extraction of lithium during the cycling process [18,25]. Interestingly, the crystal growth of MoS_2 layers exhibited a significant dependency on the structure of HPAC, resulting in curvature aligned with the hierarchical structure, as indicated by the yellow dash-line [1,23,29]. This curved growth of the MoS_2 lattice within the pores of HPAC alleviates volume expansion during lithiation and offers an abundance of edge-rich MoS_2 layers [10,23,30].

The XPS analysis was employed to investigate the chemical environment of the 1T-MoS_2/HPAC, while the obtained spectra were analyzed using the Gaussian-Lorentz method. As shown in Fig. S3, the full XPS survey confirmed the presence of molybdenum, sulfur, nitrogen, carbon, and oxygen, signifying the high purity of the 1T-MoS_2/HPAC. Moreover, a peak corresponding to sulfur vacancies was observed at 186.4 eV, providing additional active sites for lithium storage [1]. Further analysis by high resolution XPS of each element was performed for the 1T-MoS_2/HPAC.

In Fig. 3a, the deconvoluted peaks in the Mo 3p and N 1s (390–404 eV) regions showed the presence of a Mo—N bond at 396.8 eV, along with graphitic-N, pyrrolic-N, pyridinic-N, and Mo 3p peaks at 401.3, 399.8, 398.3, and 394.3 eV, respectively [1,12,31–33]. The presence of the Mo—N bond confirms the successful nitrogen doping in the molybdenum sulfide lattice [1,12,31,32]. The incorporation of graphitic-N with free electrons improved the electronic conductivity of the 1T-MoS_2/HPAC, providing better electrochemical performance [24].

The Mo 3d spectrum (Fig. 3b) exhibited two deconvoluted peaks, corresponding to the 1T-phase at 231.4 eV (Mo $3d_{3/2}$) and 228.3 eV (Mo $3d_{5/2}$) [7,25]. Additionally, the 2H-phase displayed two additional deconvoluted peaks at 232.3 and 228.9 eV [7,25]. By integrating the areas of these peaks, the percentage of 1T-phase MoS_2 was estimated to be 85 %, considering the highest reported value in the literature (Table S1). This achievement highlights the effectiveness of our methodology in obtaining a high proportion of 1T-phase MoS_2, surpassing even methods involving using other carbonaceous materials or ammonia atmosphere [24]. Furthermore, a modest peak at 234.6 eV was observed, corresponding to Mo^{6+}, possibly induced by nitrogen doping [7,31]. The presence of Mo^{6+} may contribute to enhanced internal electronic conductivity through electron transport between Mo^{6+} and Mo^{4+} during the charge/discharge process [1,32]. Additionally, a peak at 225.6 eV, attributed to S 2s, confirmed the successful synthesis of

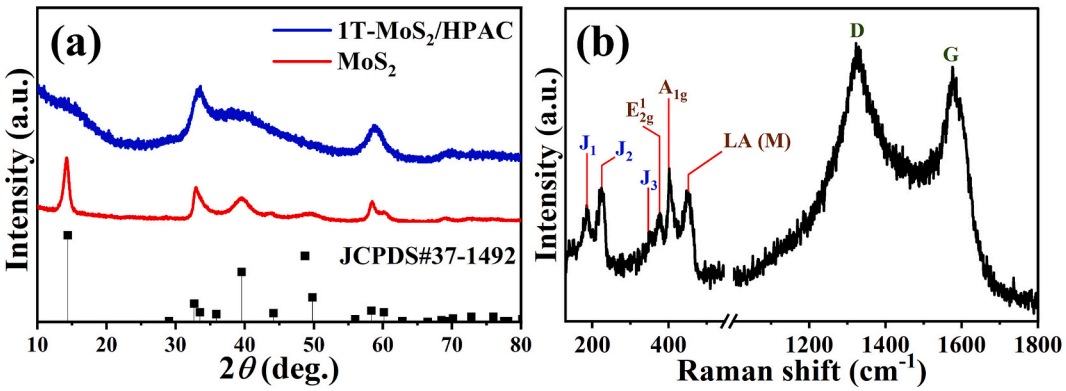

Fig. 1. (a) XRD patterns of 1T-MoS_2/HPAC and MoS_2, and (b) Raman spectrum of 1T-MoS_2/HPAC.

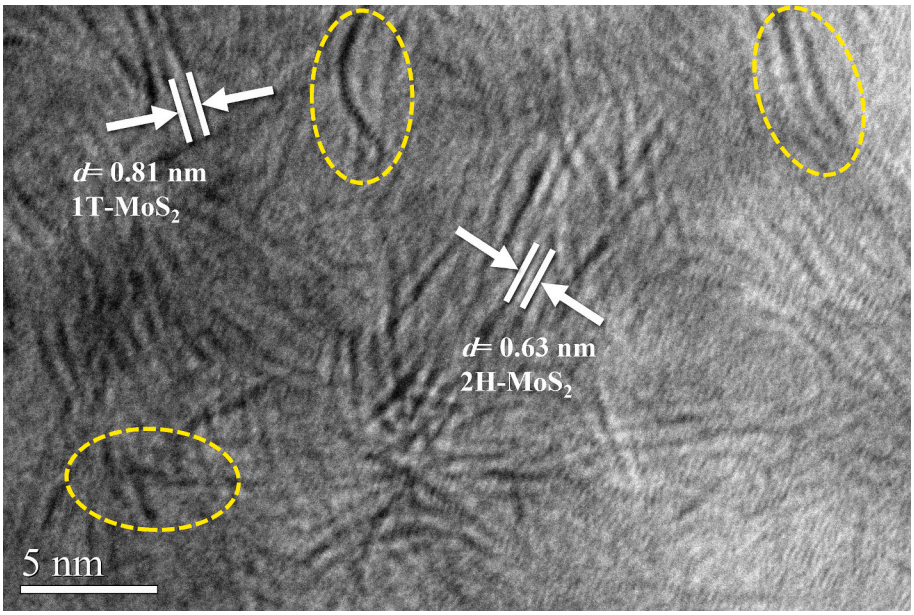

Fig. 2. High-resolution TEM micrograph of the 1T-MoS_2/HPAC. Yellow dash-line: curvature MoS_2 crystals. (For interpretation of the references to color in this figure legend, the reader is referred to the web version of this article.)

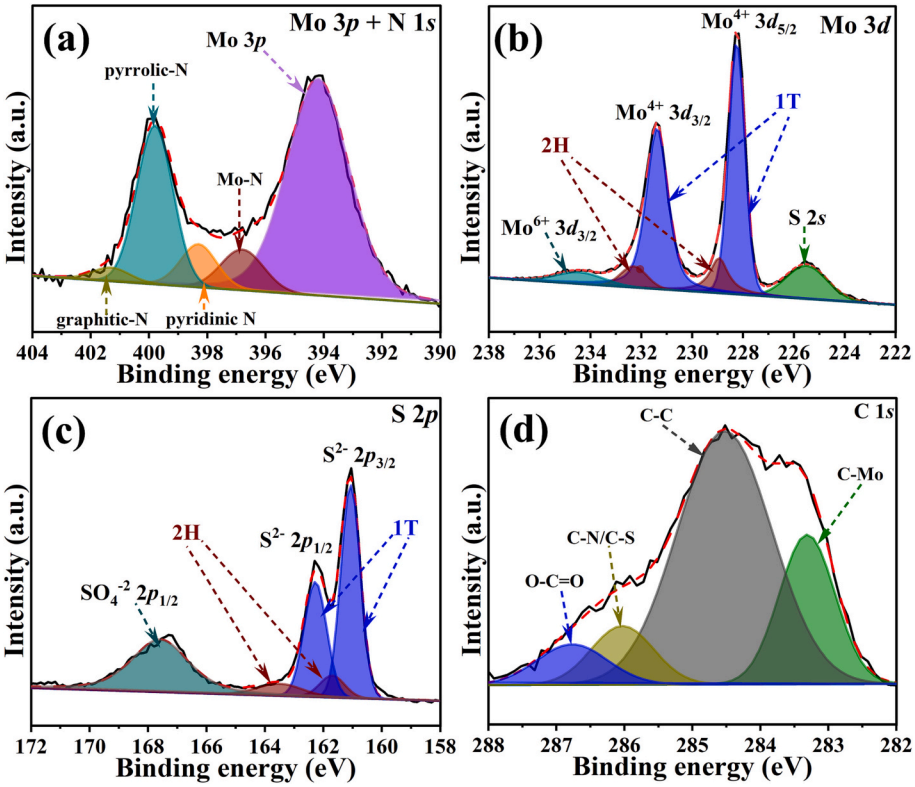

Fig. 3. High-resolution XPS spectra of 1T-MoS_2/HPAC (a) Mo 3*p* + N 1*s*, (b) Mo 3*d*, (c) S 2*p*, and (d) C 1*s* spectra.

MoS_2 [1].

In Fig. 3c, the S 2*p* spectrum displays peaks with binding energies ranging from 159 eV to 171 eV, attributed to S^{2-} in MoS_2 [1,7,33]. The deconvoluted peaks at 161.1 and 162.3 eV correspond to the 1T-phase MoS_2, whereas the peaks at 161.6 and 163.6 eV represent the 2H-phase [1,25]. Another peak at 167.5 eV was also detected, caused by the surface oxidation of sulfur [1,16]. The C 1*s* spectrum in Fig. 3d revealed the presence of a C—C bond at 284.5 eV, while a C—Mo bond appeared at 283.3 eV, confirming the interaction between HPAC and MoS_2 [33,34]. Furthermore, the deconvoluted peaks at 286.0 and 286.7 eV were ascribed to C-N/C-S and O=C-O bonds originating from the partial sulfurization of HPAC by excess thioacetamide added during synthesis process [10,20,32,35].

Elemental analyses (EA) were conducted for the 1T-MoS_2/HPAC to quantify the carbon, nitrogen, and sulfur contents. The analysis was carried out three times, and the average percentages of C, N, and S were

found to be 8.4 %, 0.9 %, and 35.4 %, respectively. The carbon originated from the activated carbon (HPAC), while the nitrogen content originates from both the HPAC and the nitrogen doped MoS_2. Nitrogen doping donates electrons to the MoS_2, improving the internal electronic conductivity and creating electroactive edges [1,36]. Sulfur content represents the sulfur in MoS_2 and the partial sulfurized HPAC during the synthesis process [10].

On the basis of evidence disclosed in this section, the 1T-MoS_2/HPAC possesses high-purity, 85 % of 1T-phase, nitrogen doping and sulfur vacancies. Consequently, it is essential to explore the formation mechanism causing such characteristics, and the electrochemical performance as well as storage mechanism for lithium-ion storage.

3.2. Formation mechanism of 1T-MoS_2/HPAC

The synthesis of the high proportion of the metallic phase (1T) MoS_2 faces a challenge due to the inherent instability 1T-MoS_2, which typically converts to the stable semiconductor phase (2H) [24,25]. Another challenge emerges from the unfavorable electrostatic interaction between the negatively charged HPAC and MoO_4^{2-}. Moreover, previous studies have demonstrated that efforts to enhance crystallinity at temperatures exceeding 200 °C prompt the transition of 1T-MoS_2 to 2H-MoS_2 phase [6,24,25]. In this study, we addressed these challenges by using ammonium molybdate as the starting material, which consists of seven ionic groups of octahedral geometry similar to the desired 1T-MoS_2 structure [18,37]. Thioacetamide was then introduced, as a mild reducing agent and sulfur source, at a controlled temperature of 150 °C to preserve the octahedral structure during the transformation from MoO_4^{2-} to MoS_2 [18]. Furthermore, an excess of thioacetamide facilitated the conversion of oxy-groups on the HPAC surface into sulfur, creating favorable nucleation sites for the growth of MoS_2 [10]. As a result, the robust interaction between partially sulfurized HPAC and the octahedral structure played a pivotal role in effectively stabilizing the 1T-phase during the subsequent calcination process at a high temperature of 550 °C for two hours. In a previous study, identical precursors were employed for the synthesis of mixed-phase MoS_2 in the absence of HPAC or any other scaffolds. The results indicated the presence of a mixed phase at 200 °C, transitioning to a pure 2H-phase upon heating to 400 °C [38]. This phase transformation observation further aligns with the findings from our XRD and micro-Raman analyses of pure MoS_2. These collective data emphasize the crucial function of HPAC in effectively stabilizing the 1T-phase during the calcination process as presented in Fig. 4.

A further approach was employed to increase the 1T-phase percentage by inducing NH_4^+ intercalation. This was accomplished by the thermal decomposition of precursors releasing NH_4^+ ions, which facilitated their *in-situ* insertion between MoS_2 layers. This intercalation, in turn, led to an expansion of the interlayer *d*-spacing and facilitated the growth of the (001) plane characteristic of the 1T-phase [1,6,24]. The NH_4^+ ions also increased the electron density in the *d* orbital of molybdenum, favoring the construction of the desired metallic phase [17,39]. Notably, the ammonium-rich precursors utilized in our method preferred to form a covalent bond between nitrogen and molybdenum, which is shorter and stronger than the bond between sulfur and molybdenum (with bond lengths of 2.03 Å and 2.43 Å, respectively) [39–41]. The nitrogen doping into the MoS_2 framework enabled the modification of its electron structures, creating sulfur vacancies and generating numerous terminal active sites [1,36,39]. Such design of 1T-MoS_2/HPAC would be beneficial for lithium storage *via* different mechanisms.

3.3. Electrochemical performance of 1T-MoS_2/HPAC

The galvanostatic measurements of the 1T-MoS_2/HPAC anode were carried out by varying the current densities from 0.1 A/g to 2.0 A/g within a potential window of 0.8 V ~ 3.0 V (*vs.* Li/Li^+) to prevent the irreversible conversion reaction [2,14–16]. By limiting the lower potential, our electrode underwent the intercalation reaction solely with lithium ions, providing the initial reversible capacity of 331 mAh/g surpasses the theoretical capacity of 167 mAh/g as represented in Fig. 5a. Previous studies have reported that MoS_2 can exhibit specific capacities exceeding the theoretical capacity of both intercalation and conversion reactions, depending on the side products of the conversion reaction [10,15]. However, for the first time, the intercalation reaction at a potential window of 0.8 V ~ 3.0 V (*vs.* Li/Li^+) delivers such exceptional capacity, exceeding other MoS_2 reference samples, including bulk, nanosheet, and composites with two-dimensional (2D) graphene nanoplatelet (GNP), as summarized in Table 1 [2,14–16]. This can be attributed to the strong affinity of lithium ions to be adsorbed on the crystalline 1T-MoS_2, nitrogen doping, sulfur vacancies, and edges [1,6,10]. In addition, the initial Coulombic efficiency of our electrode (82 %) also exceeded the majority of the reference literature [2,13–16]. Interestingly, the Coulombic efficiency of 1T-MoS_2/HPAC recovered starting from the fourth cycle, reaching 99 %. and the delivered capacities slightly increased in the second and third cycles to 337 and 339 mAh/g, respectively. The reasons for this capacity increase are discussed in the following section, supported by postmortem analysis.

During the rate capability test, the half-cell was cycled ten times each, with the final ten cycles returning to the slowest rate. The voltage profile of the last cycle at each rate is presented in Fig. 5b, exhibiting

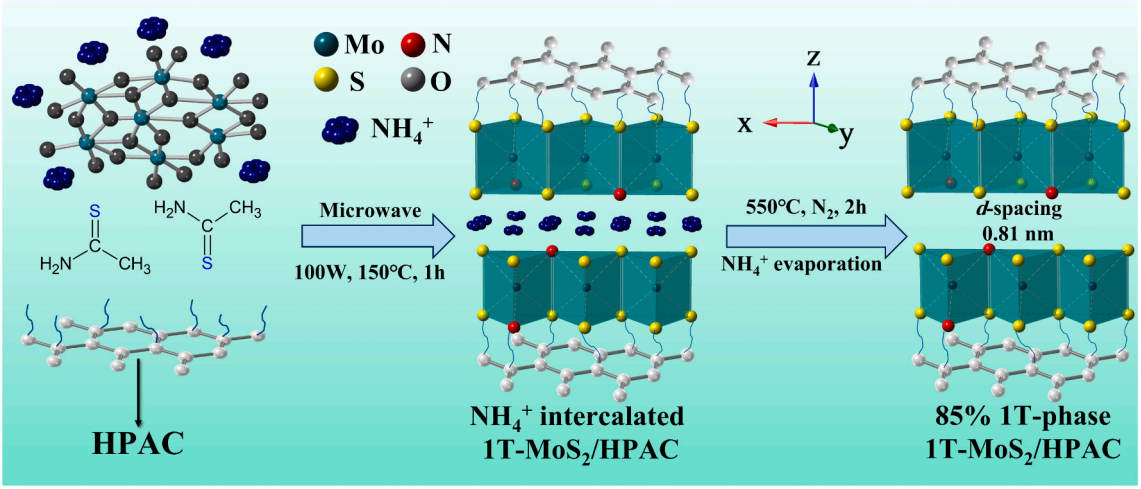

Fig. 4. Schematic diagram of the formation mechanism for 1T-MoS_2/HPAC.

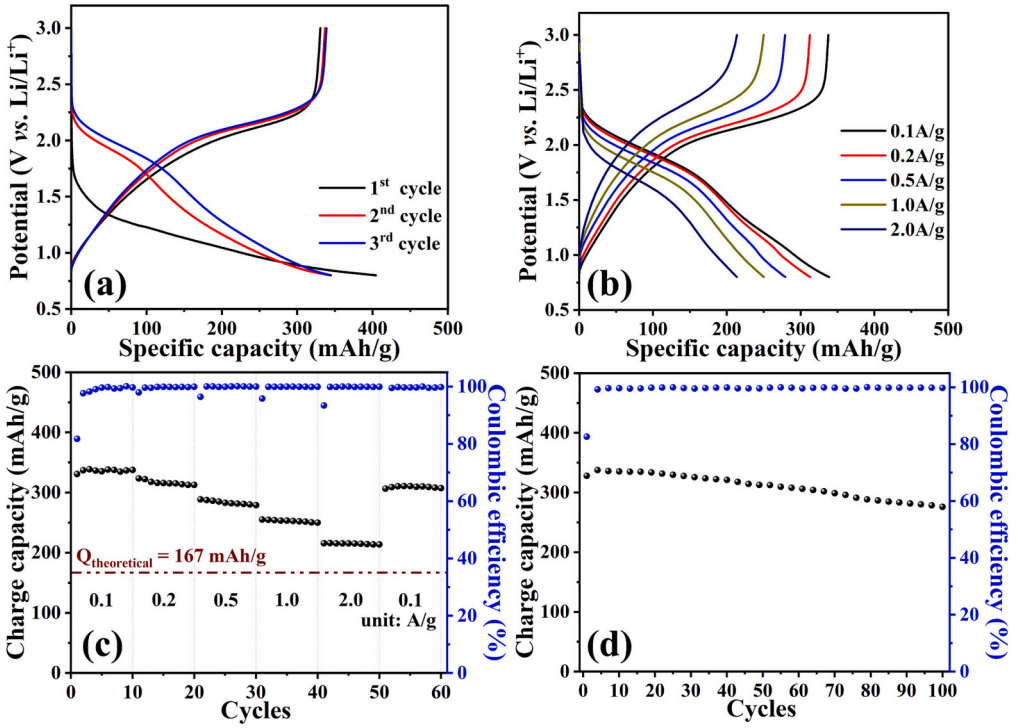

Fig. 5. Electrochemical performances of 1T-MoS_2/HPAC: (a) Galvanostatic charge-discharge profiles at 0.1 A/g, (b) Galvanostatic charge-discharge profiles recorded at the current densities from 0.1 to 2.0 A/g, (c) rate capabilities, and (d) cycling stability measured at 0.1 A/g.

Table 1
Electrochemical performance of MoS_2-based anode materials reporting in the literature at a potential window of 0.8 V ~ 3.0 V (*vs.* Li/Li^+).

Material	Initial Coulombic efficiency (%)	Initial reversible capacity (mAh/g)@0.1 A/g	Capacity retention (%)@cycles @rate
Bulk MoS_2 (commercial) [14]	68	162	83[a]@100@0.1 A/g
Nanosheet MoS_2 [15]	NA	115	91[a]@100@0.1 A/g
Nanosheet MoS_2 [2]	60[b]	191	NA
MoS_{2+x}/GNP [16]	86[a]	153	44@100@0.05 A/g
1T-MoS_2/HPAC	82	331	84@100@0.1 A/g 76@150@0.5 A/g

[a] Calculating from the data.
[b] Reading from the curves.

stable galvanostatic charge-discharge curves observed at different rates. This indicates that the 1T-MoS_2/HPAC anode underwent a consistent mechanism of lithium storage at all applied current densities [10,13]. In addition, it implies that the structure of MoS_2 was well-maintained at all rate capabilities [11,13]. Consequently, the delivered capacities continued to surpass the theoretical capacity as the rates of 0.1, 0.2, 0.5, 1.0, and 2.0 A/g, measuring 338, 313, 279, 250, and 214 mAh/g, respectively, as shown in Fig. 5c. After returning the current density to 0.1 A/g, the specific capacity was still 1.8 times higher than the theoretical capacity. To clarify the capacity contribution of HPAC within 1T-MoS_2/HPAC, the rate capabilities of HPAC were measured under the same conditions. As depicted in Fig. S4, the reversible capacity delivered from HPAC was 10.1, 8.3, 5.6, 3.0, and 1.4 mAh/g at 0.1, 0.2, 0.5, 1.0 and 2.0 A/g, respectively. Considering the low carbon percentage (8.4 %) in 1T-MoS_2/HPAC as determined by elemental analysis, it is suggested that the contribution of capacity by HPAC could be negligible. Hence, the reversible capacity of 1T-MoS_2/HPAC was mainly from the 1T-MoS_2.

EIS tests were conducted to assess the intrinsic resistance of the 1T-MoS_2/HPAC anode before and after the rate capabilities test. The Nyquist plots obtained from the impedance spectra before the test displayed a single semicircle at the high frequency and a straight line in the low-frequency region, as demonstrated in Fig. S5a. The equivalent circuit model, shown in Fig. S5b, consisted of the bulk ohmic resistance (R_b) of the entire cell in the high-frequency region, the charge-transfer resistance (R_{ct}) at the interface between the electrode and electrolyte as the diameter of the semicircle, and the diffusion element (Q_w) represents the tail at low frequency [42,43]. Subsequent to the test, a new semicircle was observed at high frequency, indicating the presence of the SEI as depicted by a new time constant in Fig. S5c [4,42]. However, the SEI resistance (R_{SEI}) minimally impacts the capacity, measuring only 2 Ω. The value of R_{ct} decreased from 43 Ω before the rate capabilities test to 12 Ω after the test, indicating enhanced ionic and electronic conductivity (Table S2).

Encouraged by the remarkable specific capacities achieved, a cycling test was conducted at 0.1 A/g, maintaining a capacity of 276 mAh/g over 100 cycles as demonstrated in Fig. 5d. These results demonstrate that our electrode can achieve remarkable reversible capacity, even after 100 cycles, surpassing the theoretical capacity. The capacity retention of 1T-MoS_2/HPAC was 84 %, comparable to the reference samples in Table 1. On the other hand, about 83 % and 76 % of capacity retentions were further noticed in Fig. S6 at 0.5 A/g for 100 and 150 cycles, respectively. Undergoing the same cycle numbers, the difference in capacity retention was almost negligible even increasing the current density to 5 times, confirming the high-rate stability of 1T-MoS_2/HPAC. The gradually capacity fading could be attributed to the volume expansion of MoS_2 during lithium intercalation, which could potentially lead to the exfoliation of MoS_2 layers [11,13].

3.4. Li^+-storage mechanism of 1T-MoS_2/HPAC

For exploring the rise in delivered capacity during the initial cycles

and to elucidate the mechanisms accountable for exceeding the theoretical capacity, CV, *ex-situ* XRD and *in-situ* EIS experiments were carried out. Fig. 6a exhibits the initial three cyclic voltammograms (CVs) of the 1T-MoS_2/HPAC electrode, employing a scanning rate of 0.2 mV/s. The first discharge displayed a broadening reduction peak starting from 2.0 V (*vs.* Li/Li^+) and ending at around 0.8 V (*vs.* Li/Li^+), signifying the occurrence of intercalation [2,13–16]. However, the following reduction peaks exhibited a positive shift to 1.9 V (*vs.* Li/Li^+) during the second and third cycles, aligning with the galvanostatic charge-discharge measurements depicted in Fig. 5a. It indicates 1T-MoS_2/HPAC was changed to a new phase (Li_xMoS_2, $1 \geq x > 0$) during the first lithiation, showing a different reduction peak position [15,44]. The oxidation peaks occurred at around 2.2 V (*vs.* Li/Li^+), representing the lithium deintercalation [15,16]. The small overpotential difference between the redox peaks in the second and third cycles (*i.e.,* 0.3 V) reveals rapid kinetic process of Li_xMoS_2, explaining the capacity enhancement in the second and third cycles [26].

The CV test was conducted at scanning rates varying from 0.2 to 5.0 mV/s, as shown in Fig. 6b. The results show that the CVs obtained at different scanning rates maintained the same characteristic shapes. This observation suggests that the pseudocapacitive lithium storage mechanism remains stable at low and high rates [10,13]. Accordingly, the 1T-MoS_2/HPAC anode exhibited a delivered capacity surpassing the theoretical capacity at all rates, as depicted in Fig. 5c. These findings demonstrate that our electrode can provide high capacity under challenging conditions [10].

To determine the contributions of the Faradic and non-Faradic processes in Li^+ storage, kinetic analysis of the collected CV curves was performed using Eq. (3), as illustrated in Fig. 6c. The analysis reveals that lithium storage is primarily governed by a surface-controlled process, ascribed to the high tendency of crystalline 1T-MoS_2 edges, nitrogen, and sulfur vacancies to adsorb lithium ions [3,4,10]. Moreover, it was observed that the lithium storage by a non-Faradic process steadily increases with increasing the scanning rates, providing high capacity at high rates [13,45]. Specifically, the contribution from the surface-controlled process increased from 71 % at 0.2 mV/s to 96 % at 5.0 mV/s, reflecting the enhanced reaction kinetics [2,28]. To investigate whether the non-Faradic storage of Li^+ is contributed by HPAC rather than 1T-MoS_2, the CV measurements of HPAC were conducted using the same conditions as 1T-MoS_2/HAPC. As illustrated in Fig. S7a, a pair of redox peaks that appeared in the potential of 0.8 V and 1.5 V (*vs.* Li/Li^+) were detected, meaning that Faradic reaction between HPAC and Li^+. However, the current density output from HPAC is significantly less than that of 1T-MoS_2/HAPC (see Fig. 6b). This shows the minor contribution of HPAC to the charge storage, which was consistent with the tendency observed in Fig. S4. Following the kinetic analysis, the capacity contribution (%) from the Faradic and non-Faradic processes was displayed in Fig. S7b. As calculated, the contribution from the non-Faradic process increased from 33 % at 0.2 mV/s to 73 % at 5.0 mV/s, reflecting the HPAC provides a significant contribution of Li^+-storage by non-Faradic process. Further considering the low carbon percentage (8.4 %) in 1T-MoS_2/HPAC as determined by elemental analysis and ~ 10 mAh/g of reversible capacity delivered from HPAC (see Fig. S4), it is suggested that the contribution of capacity by HPAC could be negligible. Based on this comprehensive analysis, it can be confidently affirmed that the Li^+-storage mechanism of 1T-MoS_2/HPAC involves both Faradic and non-Faradic reactions, with the latter being responsible for the additional capacity observed [10,13].

As observed in this study, the initial lithiation profile in both CV and galvanostatic charge-discharge tests exhibited a distinct dissimilarity compared to the subsequent cycles, implying a permanent change in the 1T-MoS_2/HPAC phase, with no restoration to its original phase. This phenomenon has been observed in numerous literature sources [1,2,15]. The differential capacity (dQ/dV) analysis, *ex-situ* XRD, and *in-situ* EIS

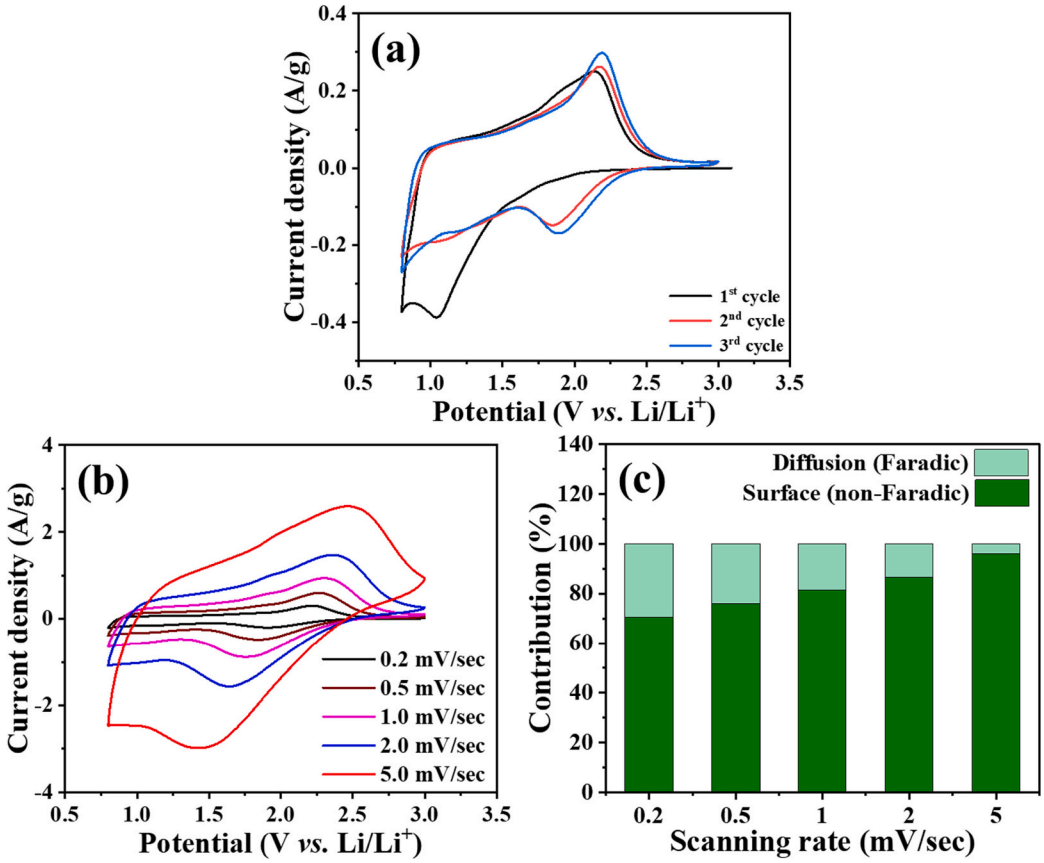

Fig. 6. (a) First three cyclic voltammograms at 0.2 mV/s, (b) cyclic voltammograms from 0.2 to 5.0 mV/s, and (c) kinetic analysis of the 1T-MoS_2/HPAC.

were conducted at different lithiation depths to study the phase transformations of 1T-MoS_2/HPAC during lithiation.

The dQ/dV analysis of the first couple of cycles was carried out, as shown in Fig. S8a. The first discharge peak was divided into three reduction peaks, with the peak current gradually increasing in the direction of lithiation until reaching its maximum value at peak (III). This suggests the lithium diffusion between 1T-MoS_2 layers (*i.e.,* intercalation) commencing at an earlier potential to produce intermediates Li_xMoS_2 compounds ($1 \geq x > 0$) through a multistep intercalation process [2,11]. In the second discharge curve, a new reduction peak appeared at 1.9 V (*vs.* Li/Li^+), and the current of both peaks (I and II) decreased sharply. This implies that one of these intermediates becomes a permanent feature after the initial lithiation and contributes to the initial Coulombic efficiency percentage [2,11,15].

Further investigation was conducted to analyze the Li_xMoS_2 using *ex-situ* XRD at various lithiation depths at 0.1 A/g, as represented in Fig. 7a. The obtained patterns demonstrate that the broadened peak observed in the fresh electrode shifted towards a lower angle following the initial lithiation at 1.3 V (*vs.* Li/Li^+), splitting into two distinct peaks. It is widely accepted that the peak occurring below a 2θ value of 10° corresponds to the (001) plane of the 1T-phase, whereas the other peak attributed to the (002) plane of the 2H-phase [2,11]. This is because the former has a higher interplanar spacing than the latter, providing better ionic/electronic conductivity [6,18,19]. By sweeping the potential to more negative direction at 1.05 V and 0.8 V (*vs.* Li/Li^+), the peak of 1T-Li_xMoS_2 consistently shifted towards a lower angle, while the peak position of 2H-Li_xMoS_2 remained unchanged. Table S3 summarizes the findings, indicating that the *d*-spacing of the (001) and (002) planes expanded to be 9.4 Å and 6.9 Å after lithiation to 0.8 V (*vs.* Li/Li^+). This signifies that the 1T-phase exhibits a considerably higher affinity for lithium intercalation than the 2H-phase, primarily due to its superior electrical conductivity, wider interplanar spacing, and high binding energy towards lithium-ion [25,45]. Notably, upon charging to 3.0 V (*vs.* Li/Li^+), no shrinking was observed in the *d*-spacing of the (001) and (002) planes, indicating the stability of Li_xMoS_2 after delithiation [2,15,45].

To assess the structure stability of Li_xMoS_2, three fresh coin cells were subjected to cycling for 2, 10, and 100 times to 3.0 V (*vs.* Li/Li^+), separately, under the same conditions. Surprisingly, the *ex-situ* XRD analysis of these disassembled electrodes revealed that the *d*-spacing of the (001) and (002) planes remained expanded as the first lithiation to 0.8 V (*vs.* Li/Li^+), as depicted in Fig. S8b, resulting in high ionic conductivity. The preservation of the unchanged *d*-spacing can be attributed to the robust stabilization of Li_xMoS_2 on the HPAC. Moreover, the hierarchal structure of the HPAC effectively constrains volume expansion, thereby maintaining the layered structure of Li_xMoS_2 during cycling [2,43,45].

The impact of phase change of 1T-MoS_2/HPAC after lithiation on the electrochemical characteristics was further investigated by *in-situ* EIS at different lithiation depths. As presented in Fig. 7b, the impedance spectra displayed distinctive behaviors at varying potentials. Fig. S9 represents the schematic diagram for the effect of lithium/delithiation on the phase transformation. Initially, as the potential was swept from OCP to 1.5 V (*vs.* Li/Li^+), lithium intercalation occurred between MoS_2 layers, combing with an adsorbed layer on the 1T-MoS_2/HPAC. Further lithiation to 0.8 V (*vs.* Li/Li^+) resulted in the formation of SEI formation with a condensed film, evident from the arc in the impedance spectra, which impeded further diffusion. During delithiation, the SEI became permanent, and the arc gradually disappeared, indicating the desorption process.

Fig. 7c presents the changes in R_b, R_{ct}, and phase angle (ϕ) obtained from fitting impedance data using the suitable model for each case (Fig. S9) [15]. Despite the formations of Li_xMoS_2 and SEI, the change in R_b was not obvious [46]. The R_{ct} increased with an increase in the lithiation depths, suggesting that the growing thickness of the lithium adsorption layer increasingly hindered the lithium transference from the electrolyte to 1T-MoS_2/HPAC [15]. In other words, the electrode surface served as a reservoir for a substantial quantity of lithium ions, particularly at 0.8 V (*vs.* Li/Li^+). Notably, the value of R_{ct} at 0.8 V (*vs.* Li/Li^+) during the first lithiation exhibited high resistance, attributed to the consumption of lithium during MoS_2 lithiation and SEI layer formation [4,13,15].

Conversely, the R_{ct} values significantly decreased during the charging process, reaching their lowest value at full delithiation (*i.e.,* at

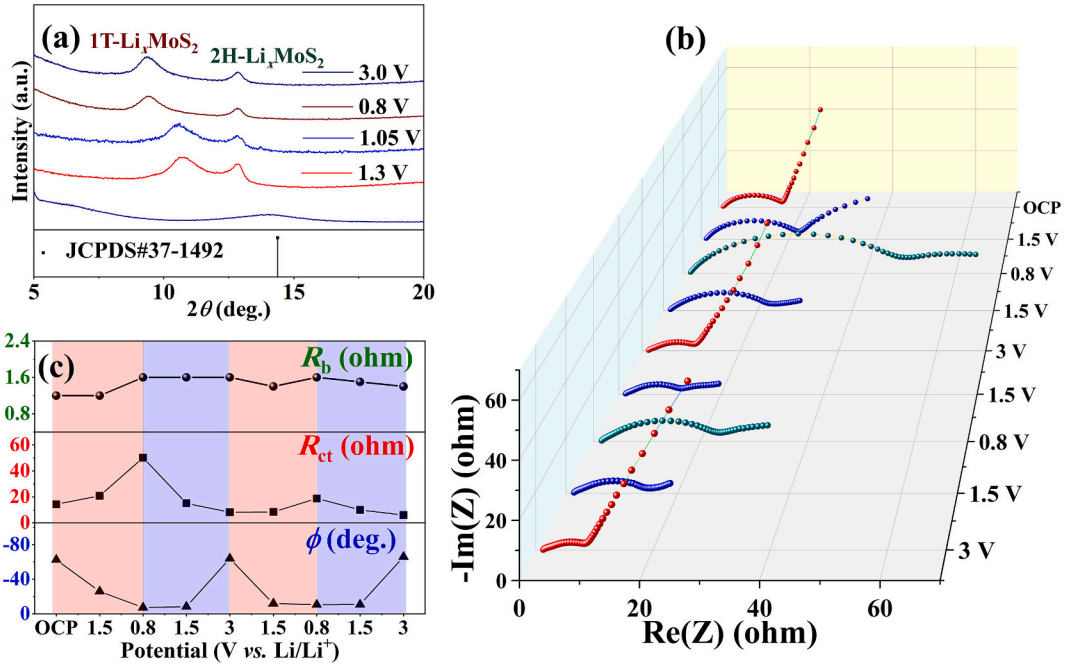

Fig. 7. (a) *Ex-situ* XRD patterns recorded for 1T-MoS_2/HPAC study at different potentials (b) *in-situ* EIS, and (c) results of fitting parameters obtained from the equivalent circuit models in Fig. S9 (Light red color: lithiation, light blue color: delithiation). (For interpretation of the references to color in this figure legend, the reader is referred to the web version of this article.)

3.0 V *vs.* Li/Li$^+$), signifying lithium desorption. This observation is supported by the phase angle of the impedance tail, which exhibited two distinct limited-diffusion behaviors. Firstly, an arc with a small phase angle appeared at 1.5 V and 0.8 V (*vs.* Li/Li$^+$), indicating limited diffusion caused by a thick adsorption layer [47]. The second type of limited diffusion occurred at the delithiated potential of 3.0 V (*vs.* Li/Li$^+$), displaying a straight line with a phase angle of approximately −62°. This indicates that no lithium ions diffused into the electrode, and the ions accumulated on the electrode surface, resembling a capacitor-like behavior [15,46,47].

Overall, the decrease in R_{ct} at 0.8 V (*vs.* Li/Li$^+$) from the first cycle to the second cycle proved that Li_xMoS_2 is more conductive than MoS_2, consistent with CV and dQ/dV plots in Fig. 6a and Fig. S8a [2,4]. This explanation is supported by the growth (001) plane of 1T-phase after the first lithiation, as shown in the *ex-situ* XRD patterns in Fig. 7a and Fig. S8b [2,4]. Consequently, the delivered specific capacity of 1T-MoS_2/HPAC increased during the initial cycles. The change in ϕ is supported by kinetic analysis of CVs, which demonstrated the remarkable lithium storage by non-Faradic process.

4. Conclusions

Benefitting from the robust interaction between the octahedral structure of the 1T-phase and HPAC, 85 % of 1T-MoS_2 was successfully achieved through the microwave-assisted method followed by the calcination process. The Li$^+$-storage mechanism has been investigated systematically in this work by restricting the potential window to maintain the crystal structure of MoS_2. Inspired by the high binding energy of Li$^+$ to the edges in the 1T-phase, along with nitrogen doping and vacancies within the MoS_2 structure, 1T-MoS_2/HPAC anode demonstrated a reversible intercalation capacity at 0.1 A/g that was two-fold greater than the theoretical capacity. Kinetic analysis revealed that adsorption-controlled processes primarily influence Li$^+$ storage in 1T-MoS_2/HPAC anodes. Further study by *ex-situ* XRD analysis unveiled the formation of a permanent phase, Li_xMoS_2, during the initial lithiation process. Moreover, the *d*-spacing of the 1T-phase expanded more than that of the 2H-phase during the initial lithiation, and both remained stable during the delithiation process even after 100 cycles. Notably, the Li_xMoS_2 showed lower overpotential and smaller charge transfer resistance than un-lithiated MoS_2, increasing the delivered capacity during the initial cycles. The demonstrated high content of 1T-phase and remarkable intercalation pseudocapacitive behavior of our 1T-MoS_2/HPAC offer distinct advantages for utilizing such materials in energy storage applications.

CRediT authorship contribution statement

Mohamed M. Abdelaal: Investigation, Formal analysis, Writing – original draft. **Chun-Chen Yang:** Resources, Writing – review & editing. **Tai-Feng Hung:** Conceptualization, Methodology, Validation, Funding acquisition, Supervision, Writing – review & editing.

Declaration of competing interest

The authors declare that they have no known competing financial interests or personal relationships that could have appeared to influence the work reported in this paper.

Data availability

Data will be made available on request.

Acknowledgements

This research was funded by the Ministry of Science and Technology (MOST) of Taiwan (grant number: MOST 110-2222-E-131-001-MY3) and Ming Chi University of Technology (grant number: VK003-6100-110).

Appendix A. Supplementary data

Supplementary data to this article can be found online at https://doi.org/10.1016/j.est.2023.109926.

References

[1] A. Kotsun, V. Alekseev, S. Stolyarova, A. Makarova, M. Grebenkina, A. Zubareva, A. Okotrub, L. Bulusheva, Effect of molybdenum disulfide doping with substitutional nitrogen and sulfur vacancies on lithium intercalation, J. Alloys Compd. 947 (2023), 169689, https://doi.org/10.1016/j.jallcom.2023.169689.
[2] C. Quilty, L. Housel, D. Bock, M. Dunkin, L. Wang, D. Lutz, A. Abraham, A. Bruck, E. Takeuchi, K. Takeuchi, A. Marschilok, Ex situ and operando XRD and XAS analysis of MoS_2: a lithiation study of bulk and nanosheet materials, ACS Appl. Energy Mater. 2 (2019) 7635–7646, https://doi.org/10.1021/acsaem.9b01538.
[3] Z. Gan, L. Liu, P. Hai, L. Li, Y. Gao, J. Yin, M. Li, C. Wu, W. Ai, Y. Cheng, X. Xu, Unleash sodium storage potential of MoS_2 nanosheets: generating favorable kinetics from optimal crystallinity and elaborate structure, J. Power Sources 570 (2023), 233028, https://doi.org/10.1016/j.jpowsour.2023.233028.
[4] J. Cook, H. Kim, T. Lin, C. Lai, B. Dunn, S. Tolbert, Pseudocapacitive charge storage in thick composite MoS_2 nanocrystal-based electrodes, Adv. Energy Mater. 7 (2017) 1601283, https://doi.org/10.1002/aenm.201601283.
[5] H. Tian, M. Yu, X. Liu, J. Qian, W. Qian, Z. Chen, Z. Wu, Plant-cell oriented few-layer MoS_2/C as high performance anodes for lithium-ion batteries, Electrochim. Acta 424 (2022), 140685, https://doi.org/10.1016/j.electacta.2022.140685.
[6] Z. Lei, J. Zhan, L. Tang, Y. Zhang, Y. Wang, Recent development of metallic (1T) phase of molybdenum disulfide for energy conversion and storage, Adv. Energy Mater. 8 (2018) 1703482, https://doi.org/10.1002/aenm.201703482.
[7] E. Yang, N. Wei, M. Li, R. Xu, Y. Sui, M. Kong, X. Ran, H. Cui, Three-dimensional artificial transpiration structure based on 1T/2H-MoS_2/activated carbon fiber cloth for solar steam generation, ACS Appl. Mater. Interfaces 14 (2022) 29788–29796, https://doi.org/10.1021/acsami.2c05306.
[8] S. Shi, Z. Sun, Y.H. Hu, Synthesis, stabilization and applications of 2-dimensional 1T metallic MoS_2, J. Mater. Chem. A 6 (2018) 23932–23977, https://doi.org/10.1039/C8TA08152B.
[9] R. Sha, T. Bhattacharyya, MoS_2-based nanosensors in biomedical and environmental monitoring applications, Electrochim. Acta 349 (2020), 136370, https://doi.org/10.1016/j.electacta.2020.136370.
[10] L. Wang, Q. Zhang, J. Zhu, X. Duan, Z. Xu, Y. Liu, H. Yang, B. Lu, Nature of extra capacity in MoS_2 electrodes: molybdenum atoms accommodate with lithium, Energy Storage Mater. 16 (2019) 37–45, https://doi.org/10.1016/j.ensm.2018.04.025.
[11] G. Wang, Y. Zhang, H.S. Cho, X. Zhao, F. Kim, J. Zou, Revisiting the structural evolution of MoS_2 during alkali metal (Li, Na, and K) intercalation, ACS Appl. Energy Mater. 4 (2021) 14180–14190, https://doi.org/10.1021/acsaem.1c02937.
[12] W. Jia, H. Wu, Y. Zheng, Z. Liu, G. Cai, J. Wen, G. Hu, T. Tang, X. Li, L. Jiang, Z. Wang, M. Li, H. Huang, Co/N Co-doped MoS_2 with high pseudocapacitive performance for solid-state flexible supercapacitors, ACS Appl. Energy Mater. 6 (2023) 2570–2581, https://doi.org/10.1021/acsaem.2c04044.
[13] K. Zhang, G. Yoon, J. Zhang, M. Park, J. Yang, K. Kang, Y. Kang, Pseudocapacitive behavior and ultrafast kinetics from solvated ion cointercalation into MoS_2 for its alkali ion storage, ACS Appl. Energy Mater. 2 (2019) 3726–3735, https://doi.org/10.1021/acsaem.9b00445.
[14] L. Zhang, D. Sun, J. Kang, J. Feng, H. Bechtel, L. Wang, E. Cairns, J. Guo, Electrochemical reaction mechanism of the MoS_2 electrode in a lithium-ion cell revealed by in situ and operando X-ray absorption spectroscopy, Nano Lett. 18 (2018) 1466–1475, https://doi.org/10.1021/acs.nanolett.7b05246.
[15] C. Deng, H. Wang, S. Wang, Clarifying the lithium storage behavior of MoS_2 with in situ electrochemical impedance spectroscopy, J. Mater. Chem. A 9 (2021) 15734–15743, https://doi.org/10.1039/D1TA02517A.
[16] D. Lutz, M. Dunkin, S. King, C. Stackhouse, J. Kuang, Y. Du, S. Bak, D. Bock, X. Tong, L. Ma, S. Ehrlich, E. Takeuchi, K. Takeuchi, A. Marschilok, L. Wang, Hybrid MoS_{2+x} nanosheet/nanocarbon heterostructures for lithium-ion batteries, ACS Appl. Nano Mater. 5 (2022) 5103–5118, https://doi.org/10.1021/acsanm.2c00141.
[17] I. Kwak, I. Kwon, H. Abbas, G. Jung, Y. Lee, J. Park, H. Kang, Stable methylammonium-intercalated 1T′-MoS_2 for efficient electrocatalytic hydrogen evolution, J. Mater. Chem. A 6 (2018) 5613–5617, https://doi.org/10.1039/C8TA00700D.
[18] Y. Jiao, A. Hafez, D. Cao, A. Mukhopadhyay, Y. Ma, H. Zhu, Metallic MoS_2 for high performance energy storage and energy conversion, Small 14 (2018) 1800640, https://doi.org/10.1002/smll.201800640.
[19] M. Wu, J. Zhan, K. Wu, Z. Li, L. Wang, B. Geng, L. Wang, D. Pan, Metallic 1T MoS_2 nanosheet arrays vertically grown on activated carbon fiber cloth for enhanced Li-ion storage performance, J. Mater. Chem. A 5 (2017) 14061–14069, https://doi.org/10.1039/C7TA03497K.
[20] M. Abdelaal, T. Hung, S. Mohamed, C. Yang, T. Hung, Two birds with one stone: hydrogel-derived hierarchical porous activated carbon toward the capacitive performance for symmetric supercapacitors and lithium-ion capacitors, ACS

Sustain. Chem. Eng. 10 (2022) 4717–4727, https://doi.org/10.1021/acssuschemeng.2c00266.
[21] J. Jiang, Y. Zhang, Y. An, L. Wu, Q. Zhu, H. Dou, X. Zhang, Engineering ultrathin MoS_2 nanosheets anchored on N-doped carbon microspheres with pseudocapacitive properties for high-performance lithium-ion capacitors, Small Methods 3 (2019), 1900081, https://doi.org/10.1002/smtd.201900081.
[22] H. Gao, J. Zang, Y. Wang, S. Zhou, P. Tian, S. Song, X. Tian, W. Li, One-step preparation of cobalt-doped NiS@MoS_2 core-shell nanorods as bifunctional electrocatalyst for overall water splitting, Electrochim. Acta 377 (2021), 138051, https://doi.org/10.1016/j.electacta.2021.138051.
[23] J. Yang, S. Tang, Q. Yang, Z. Liu, C. Liu, Y. Wu, Z. Li, R. Zhu, W. Jiang, P. He, X. Si, F. Zhang, Z. Liu, Confined growth of 3D ordered, highly curved MoS_2 frameworks for superior lithium-ion storage, Mater. Lett. 347 (2023), 134540, https://doi.org/10.1016/j.matlet.2023.134540.
[24] Y. Zhou, Y. Liu, M. Zhang, Q. Han, Y. Wang, X. Sun, X. Zhang, C. Dong, J. Sun, Z. Tang, F. Jiang, Rationally designed hierarchical N, P co-doped carbon connected 1T/2H-MoS_2 heterostructures with cooperative effect as ultrafast and durable anode materials for efficient sodium storage, Chem. Eng. J. 433 (2022), 133778, https://doi.org/10.1016/j.cej.2021.133778.
[25] J. Wang, L. Sun, H. Tan, F. Xie, Y. Qu, J. Hu, K. Gao, X. Shi, K. Wang, Y. Zhang, Double-phase 1T/2H-MoS_2 heterostructure loaded in N-doped carbon/CNT complex carbon for efficient and rapid lithium storage, Mater. Today Energy 29 (2022), 101103, https://doi.org/10.1016/j.mtener.2022.101103.
[26] W. Liao, T. Hung, M. Abdelaal, C. Chao, C. Fang, S. Mohamed, C. Yang, Highly efficient sodium-ion capacitor enabled by mesoporous $NaTi_2(PO_4)_3$/C anode and hydrogel-derived hierarchical porous activated carbon cathode, J. Energy Storage 55 (2022), 105719, https://doi.org/10.1016/j.est.2022.105719.
[27] R. Amirtha, H. Hsu, M. Abdelaal, A. Anbunathan, S. Mohamed, C. Yang, T. Hung, Constructing a carbon-encapsulated carbon composite material with hierarchically porous architectures for efficient capacitive storage in organic supercapacitors, Int. J. Mol. Sci. 23 (2022) 6774, https://doi.org/10.3390/ijms23126774.
[28] M. Abdelaal, H. Hsu, W. Liao, S.G. Mohamed, C. Yang, T. Hung, Hierarchical porous activated carbon anode for dual carbon lithium-ion capacitors: energy storage mechanisms and electrochemical performances, J. Taiwan Inst. Chem. Eng. 104912 (2023), https://doi.org/10.1016/j.jtice.2023.104912.
[29] A. Chouhan, T. Sarkar, S. Kumari, S. Vemuluri, O. Khatri, Synergistic lubrication performance by incommensurately stacked ZnO-decorated reduced graphene oxide/MoS_2 heterostructure, J. Colloid Interface Sci. 580 (2020) 730–739, https://doi.org/10.1016/j.jcis.2020.07.033.
[30] J. Lin, Y. Shi, Y. Li, X. Wu, J. Zhang, H. Xie, H. Sun, Confined MoS_2 growth in a unique composite matrix for ultra-stable and high-rate lithium/sodium-ion anodes, Chem. Eng. J. 428 (2022), 131103, https://doi.org/10.1016/j.cej.2021.131103.
[31] H. Lim, H. Kim, S. Kim, W. Choi, Self-assembled N-doped MoS_2/carbon spheres by naturally occurring acid-catalyzed reaction for improved sodium-ion batteries, Chem. Eng. J. 387 (2020), 124144, https://doi.org/10.1016/j.cej.2020.124144.
[32] J. Jiao, K. Du, Y. Wang, P. Sun, H. Zhao, P. Tang, Q. Fan, H. Tian, Q. Li, Q. Xu, N plasma treatment on graphene oxide-MoS_2 composites for improved performance in lithium ion batteries, Mater. Chem. Phys. 240 (2020), 122169, https://doi.org/10.1016/j.matchemphys.2019.122169.
[33] H. Wei, Q. Xi, X. Chen, D. Guo, F. Ding, Z. Yang, S. Wang, J. Li, S. Huang, Molybdenum carbide nanoparticles coated into the graphene wrapping N-doped porous carbon microspheres for highly efficient electrocatalytic hydrogen evolution both in acidic and alkaline media, Adv. Sci. 5 (2018), 1700733, https://doi.org/10.1002/advs.201700733.
[34] L. Jia, B. Liu, Y. Zhao, W. Chen, D. Mou, J. Fu, Y. Wang, W. Xin, L. Zhao, Structure design of MoS_2@Mo_2C on nitrogen-doped carbon for enhanced alkaline hydrogen evolution reaction, J. Mater. Sci. 55 (2020) 16197–16210, https://doi.org/10.1007/s10853-020-05107-2.
[35] M. Abdelaal, T. Hung, S. Mohamed, C. Yang, H. Huang, T. Hung, A comparative study of the influence of nitrogen content and structural characteristics of NiS/nitrogen-doped carbon nanocomposites on capacitive performances in alkaline medium, Nanomaterials 11 (2021) 1867, https://doi.org/10.3390/nano11071867.
[36] K. Lv, W. Suo, M. Shao, Y. Zhu, X. Wang, J. Feng, M. Fang, Y. Zhu, Nitrogen doped MoS_2 and nitrogen doped carbon dots composite catalyst for electroreduction CO_2 to CO with high Faradaic efficiency, Nano Energy 63 (2019), 103834, https://doi.org/10.1016/j.nanoen.2019.06.030.
[37] X. Guo, Z. Wang, W. Zhu, H. Yang, The novel and facile preparation of multilayer MoS_2 crystals by a chelation-assisted sol-gel method and their electrochemical performance, RSC Adv. 7 (2017) 9009–9014, https://doi.org/10.1039/C6RA25558B.
[38] F. Shao, Y. Huang, X. Wang, Z. Li, X. Huang, W. Huang, L. Dong, F. Kang, W. Liu, C. Xu, MoS_2 with high 1T phase content enables fast reversible zinc-ion storage via pseudocapacitance, Chem. Eng. J. 448 (2022), 137688, https://doi.org/10.1016/j.cej.2022.137688.
[39] K. Le, X. Zhang, Q. Zhao, Y. Liu, P. Yi, S. Xu, W. Liu, Controllably doping nitrogen into 1T/2H MoS_2 heterostructure nanosheets for enhanced supercapacitive and electrocatalytic performance by low-power N_2 plasma, ACS Appl. Mater. Interfaces 13 (2021) 44427–44439, https://doi.org/10.1021/acsami.1c12973.
[40] Q. Yang, Z. Wang, L. Dong, W. Zhao, Y. Jin, L. Fang, B. Hu, M. Dong, Activating MoS_2 with super-high nitrogen-doping concentration as efficient catalyst for hydrogen evolution reaction, J. Phys. Chem. C 123 (2019) 10917–10925, https://doi.org/10.1021/acs.jpcc.9b00059.
[41] H. Wu, Y. Qian, R. Lu, W. Tan, A theoretical study on the electronic property of a new two-dimensional material molybdenum dinitride, Phys. Lett. A 380 (2016) 768–772, https://doi.org/10.1016/j.physleta.2015.12.017.
[42] T. Sahu, S. Mitra, Exfoliated MoS_2 sheets and reduced graphene oxide-an excellent and fast anode for sodium-ion battery, Sci. Rep. 5 (2015) 12571, https://doi.org/10.1038/srep12571.
[43] J. Ju, L. Zhang, H. Shi, Z. Li, W. Kang, B. Cheng, Three-dimensional porous carbon nanofiber loading MoS_2 nanoflake-flowerballs as a high-performance anode material for Li-ion capacitor, Appl. Surf. Sci. 484 (2019) 392–402, https://doi.org/10.1016/j.apsusc.2019.04.099.
[44] X. Fang, C. Hua, X. Guo, Y. Hu, Z. Wang, X. Gao, F. Wu, J. Wang, L. Chen, Lithium storage in commercial MoS_2 in different potential ranges, Electrochim. Acta 81 (2012) 155–160, https://doi.org/10.1016/j.electacta.2012.07.020.
[45] Y. Zhu, H. Li, Y. Wu, L. Yang, Y. Sun, G. Chen, Y. Liu, Z. Wu, C. Zhang, X. Guo, Unveiling the abnormal capacity rising mechanism of MoS_2 anode during long-term cycling for sodium-ion batteries, RSC Adv. 11 (2021) 28488–28495, https://doi.org/10.1039/D1RA05518F.
[46] X. Zhang, X. Zhang, X. Sun, Y. An, S. Song, C. Li, K. Wang, F. Su, C. Chen, F. Liu, Z. Wu, Y. Ma, Electrochemical impedance spectroscopy study of lithium-ion capacitors: modeling and capacity fading mechanism, J. Power Sources 488 (2021), 229454, https://doi.org/10.1016/j.jpowsour.2021.229454.
[47] M. Oldenburger, B. Bedürftig, A. Gruhle, F. Grimsmann, E. Richter, R. Findeisen, A. Hintennach, Investigation of the low frequency Warburg impedance of Li-ion cells by frequency domain measurements, J. Energy Storage 21 (2019) 272–280, https://doi.org/10.1016/j.est.2018.11.029.